Modeling Radar Scatter from Distributed Targets Using a Coupled Scatterer Approach

Peter J. F. Swart and Paul Snoeij

***Abstract*—Radar remote sensing deals with the extraction of object information from electromagnetic wave parameters. To fully exploit the potential of acquiring quantitative information requires a detailed description of the interaction between microwaves and objects. For practical reasons a simplified approach is preferred where the radar return of a distributed target is modeled as a sum of scatterer echoes.**

In this paper, a point scatterer model is given to simulate scattering of radar waves by distributed targets. The scatterers may have different heights in synthesizing rough surfaces. The principle of conservation of energy is used to account for electromagnetic coupling between the scatterers in function of target sampling density. The predicted coupling between two scatterers is experimentally verified by indoor radar cross section measurements. The model is verified through comparison with numerically solving the electric field integral equation for linear scatterer arrays. Results are given in the form of bistatic scatter diagrams to provide insight in the full scattering behavior.

I. Introduction

The radar cross section σ is defined for a single target as a hypothetical area intercepting that amount of power, which, when scattered isotropically, produces an echo with the same power as received from the actual object. A distributed target consists of many point scatterer targets whose locations are fairly random. The radar return is characterized by the average radar cross section per unit area, σ^0 [1]. The consequences of using the concept of σ^0 even in the presence of partial coherency are given in [2] based on a discretized representation of the scattering process as in [3]. With this a scatterer model is derived for distributed targets. Coupling between the model scatterers is implemented by use of the energy conservation requirement. Only the lossless case is considered.

First a two-dimensional model, based on coupled point scatterers, is presented and applied to a flat plate. An example shows the effect of introducing roughness on scattering angle dependency. Then a one-dimensional version of the model, using coupled line scatterers, is given and the general behavior of the results and dependence on model parameters is discussed. The coupling between two line scatterers was experimentally verified and measurement results are shown. Model verification is supported by results obtained from solving the electric field integral equation using the moment method, examples of which are given.

Manuscript received July 20, 1992; revised July 12, 1993. This work was supported by the Netherlands Remote Sensing Board.

The authors are with the Laboratory of Telecommunication and Remote Sensing Technology, Department of Electrical Engineering, Delft University of Technology 2600 GA Delft, The Netherlands.

IEEE Log Number 9215113

II. Two-Dimensional Model

A distributed target or more specifically a surface is represented by a collection of individual so called point scatterers, i.e., they have no physical size, which are assumed to be isotropically scattering as long as the distance between them is large compared to the radar wavelength. The continuous case however demands that the point scatterers may become infinitesimally closely spaced. The dependence on spacing distance is related to the electromagnetic coupling between the scatterers. The principle of conservation of energy is applied to provide for this coupling, where it is assumed that there are no losses.

The derivation of the point scatterer model is presented in Appendix I. Using a square grid of N by N equidistant identical point scatterers the monostatic radar cross section normalized with respect to the total point scatterer cross section is given, in accordance with (A18) and $\theta' = \theta$, by

$$\sigma_{CSM(2)}(\theta) = \frac{N^2 + 2\Sigma\Sigma \cos 2\Delta I}{N^2 + 2\Sigma\Sigma \cos \Delta I \left(\dfrac{\sin \Delta R}{\Delta R}\right)} \tag{1}$$

with

$$\begin{aligned} N^2 &= K, \text{ the total number of point scatterers} \\ \Delta I &= \beta(\Delta x \sin \theta + \Delta z \cos \theta) \\ \Delta R &= \beta \sqrt{(\Delta x^2 + \Delta y^2 + \Delta z^2)} \\ \Delta x &= d_{ai} - d_{ai'} \\ \Delta y &= d_{bj} - d_{bj'} \\ \Delta z &= h_k - h_{k'} \\ d_a &= d_b = d = a/N, \qquad a = \text{side-length} \end{aligned} \tag{2}$$

where $\beta = 2\pi/\lambda$ with λ the radar wavelength, and the other variables as defined in Appendix I. The double summation in (1) stretches out over all point pair combinations so that there are $\frac{1}{2}N^2(N^2 - 1)$ summation terms. The point scatterers are given different heights in synthesizing rough surfaces.

It is noted that the point scatterer model describes the scattering from discretized surfaces, and the transition to

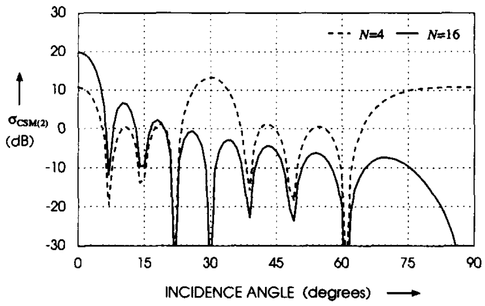

Fig. 1. Flat plate simulation result in dB, side-length $a = 4\lambda$.

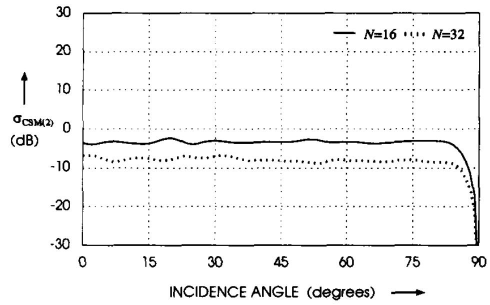

Fig. 2. Two-dimensional model result in dB, $a = 4\lambda$, roughness $s = \lambda$, averaged 100 realizations.

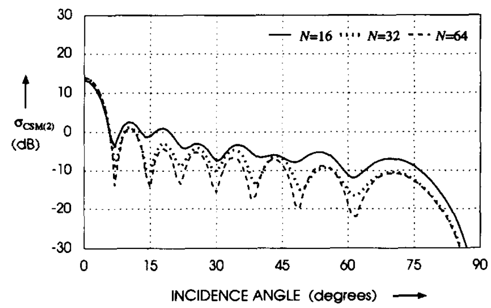

Fig. 3. Two-dimensional model result in dB, $a = 4\lambda$, roughness $s = 0.1\lambda$, averaged 10 realizations.

the continuous case is not actually made. The model rather focuses on the summation process of supposed scatterer contributions into the scattered field. Nevertheless its formulation is closely related to the numerical presentation of the general Kirchhoff solution for a perfectly conducting surface given in [3] as becomes clear from the simple case in absence of roughness described below.

A. Flat Plate

The radar cross section of a perfectly conducting square flat plate is approximately given by Physical Optics (P.O.) [4]. The angular dependence follows the well-known diffraction pattern. Fig. 1 gives the model result for a square plate with side-length $a = 4\lambda$ sampled with $N = 4$, resp., $N = 16$. It is noted that the 4λ side implies P.O. to be valid only for $\theta < 40°$. The $\lambda/4$ sampling suffices for the model result to agree with the P.O. result of the continuous flat plate except for a factor $2\cos^2\theta$. The factor $\cos^2\theta$ is the two-way projection of the incident field on the plate surface. The factor 2 is caused by the point scatterer surface being transparent even if the point density becomes infinite. The value of $\sigma_{CSM(2)}$ for $\theta = 0$ degrees increases monotonically for decreasing point spacing d, for $d < \lambda/2$, towards half the P.O. limit.

B. Surface Roughness

If roughness is introduced, average scatter values can be determined from repeated simulation for a sufficiently large number of statistically independent roughness realizations. Fig. 2 shows the result for uniformly distributed point scatterer height variations with standard deviation $s = \lambda$, $a = 4\lambda$, $N = 16$ and 32, and averaging over 100 realizations. The latter value is sufficiently large for the results not to change significantly upon further increasing the number of averages. In this case the value of $s = \lambda$ must be considered already large as it causes the backscatter to become more or less angle independent. Furthermore Fig. 2 shows that an increase of N results in an overall decrease of the backscatter level in this case.

Decreasing the roughness parameter to $s = 0.1\lambda$ leads to Fig. 3. The decrease of roughness allows for a reduced number of averages to suffice, in this case it is over 10 realizations. Also the case with $N = 64$ is considered. It is clear that the dependency on N is related to the measure of incoherency of the backscatter signal depending on the angle of incidence. This may be generalized by considering the bistatic scatter case, see Section III-B.

III. One-Dimensional Model

The one-dimensional model geometry is given in Fig. 4. It consists of a one-dimensional grid containing N equally spaced identical line scatterers. In close analogy to the two-dimensional model, the monostatic radar cross section normalized with respect to the total line scatterer cross section that follows from Appendix II is given by

$$\sigma_{CSM(1)}(\theta) = \frac{N + 2\Sigma\Sigma \cos 2\Delta I}{N + 2\Sigma\Sigma \cos \Delta I\,(J_0(\Delta R))}. \tag{3}$$

As an example Fig. 1 was reproduced using (3) instead of (1) resulting in Fig. 5 where the length $L = 4\lambda$ and $N = 4$, resp., $N = 16$. The main difference is that the value at normal incidence for large N approaches $\pi L/\lambda$ (=11 dB) where the two-dimensional case leads to $2\pi a^2/\lambda^2$ (=20 dB).

At this point it is recognized that continued simulation using (3) and interpretation of results will benefit from insight in the general behavior of the model. The angle dependence of (3) is found to be mainly due to the numerator. This is caused by the relatively fast fluctuating phasefactor $2\Delta I$ as a function of θ in the numerator compared to ΔI in the denominator. Additionally the denominator its angle dependence is counteracted by $J_0(\Delta R)$. In the following treating them separately, despite that this is

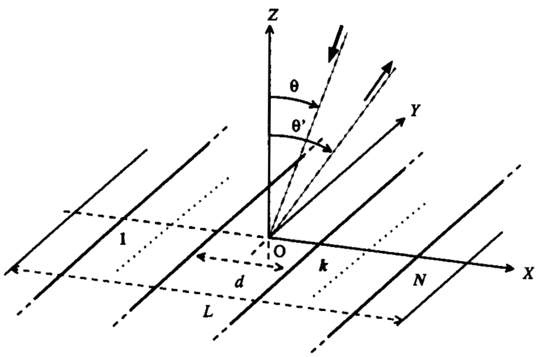

Fig. 4. One-dimensional, line scatterer, model geometry.

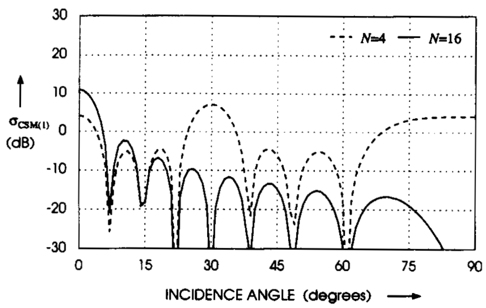

Fig. 5. One-dimensional simulation result in dB, length $L = 4\lambda$, no roughness.

an approximation, is pursued since it reveals characteristics of the model solution.

A. Statistical Description

The probability density function of the numerator in (3) follows from the rough surface statistics only after the model parameters L, N, θ are given specific settings. This already requires numerical calculations to take place over a large number of surface realizations. Therefore it is generally not feasible to state the outcome for certain surface descriptions in terms of the model parameters. An exception to this is formed by the average result over a large number of realizations where one may write

$$\langle \Sigma\Sigma \cos 2\Delta I \rangle = \langle \cos 2Z \rangle \Sigma\Sigma \cos 2X - \langle \sin 2Z \rangle \Sigma\Sigma \sin 2X \qquad (4)$$

in which $\langle \; \rangle$ denotes the ensemble average which for the double summation in the numerator of (3) is written in function of stochastic parts with

$$Z = \beta \Delta z \cos \theta \qquad (5)$$

and deterministic parts with

$$X = \beta \Delta x \sin \theta. \qquad (6)$$

The deterministic parts in (4) can be rewritten as single summations by collecting equal distance differences Δx between two line scatterers k and k' where $1 < k < k' < N$, it follows:

$$\sum_{k=1}^{N} \sum_{k'=k+1}^{N} \cos 2X = \sum_{(k'-k)=1}^{N-1} (N - (k' - k)) \cos (2\beta \Delta x \sin \theta) = \int_{-d/2}^{-L+d/2} - \left(N + \frac{\Delta x}{d}\right) \cos (2\beta \Delta x \sin \theta) \frac{d(\Delta x)}{d} \qquad (7)$$

and likewise for $\sin 2X$. The transition to the integral representation above is based on

$$\Delta x = -(k' - k)\, d$$
$$d(\Delta x) = -d = -L/N$$

where N is assumed to be large as it should already be to provide sufficient surface sampling. Solving the integral in (7) leads to

$$\Sigma\Sigma \cos 2X = \tfrac{1}{2} N^2 \{(\sin u)/u\}^2 - \tfrac{1}{2} N, \quad \text{with } u = \beta L \sin \theta \qquad (8)$$

and the sine part is likewise found to become

$$\Sigma\Sigma \sin 2X = \frac{1}{2u} N^2 \{(\sin 2u)/2u\} - \frac{1}{2u} N^2. \qquad (9)$$

For the trivial case in the absence of line scatterer height differences it follows from substituting (8) in (3) that the numerator of (3) then equals $N^2 \{(\sin u)/u\}^2$ with the factor N^2 due to the coherent summation process and the $\{(\sin u)/u\}^2$ part is recognized as the earlier mentioned well known diffraction pattern (Fig. 1). In case of large roughness the stochastic parts in (4) will be zero on average as will become clear from the example in case of Gaussian roughness given below. The numerator of (3) then equals N due to power summation and the result is no longer angle dependent.

The stochastic parts in (4) require knowledge of the statistics. As an example the line height is assumed to be Gaussian distributed with zero average and standard deviation s. In this case simply the same distribution yields for the height difference Δz between two arbitrary lines and if their respective heights are statistically independent the standard deviation is $s\sqrt{2}$. The stochastic variable Z follows from (5). Finally the distribution of the cosine and sine functions of $2Z$ may be calculated for specific values of s.

Examples are given in Figs. 6(a) and (b) for the cosine and sine results for $s = 0.03\lambda$ and $s = 0.3\lambda$ with $\theta = 45$ degrees. From this it is concluded that here $s = 0.03\lambda$ represents relatively small roughness resulting in an asymmetric cosine distribution and a near Gaussian sine distribution corresponding to their small arguments. On the other hand $s = 0.3\lambda$ represents rather large roughness

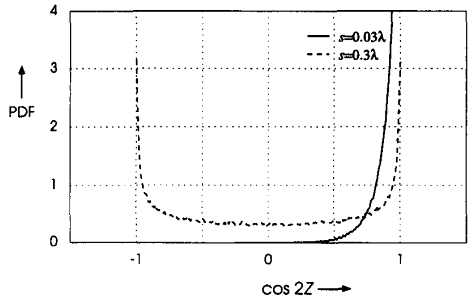

(a)

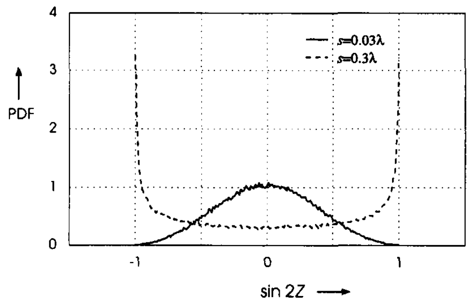

(b)

Fig. 6. (a) Probability density function (PDF) of cos (2Z), with $Z = 2\pi/\lambda(\Delta z \cos\theta)$ and z Gaussian with standard deviation s, (b) idem, sin (2Z).

where cosine and sine distributions both converge to

$$p(f) = \frac{1}{\pi\sqrt{1 - f^2}} \tag{10}$$

and f denotes the cosine, respectively, sine of a variable that is uniformly distributed over a 2π interval. The latter distribution is seen to be symmetrical around the origin resulting in zero average. It is concluded that more generally given a symmetrical line height distribution the right-hand side of (4) is only nonzero by the cosine term and large roughness implies (4) to become zero whatever the distribution.

B. Normalization

It is explained in Appendix II that the denominator of (3) is in fact a normalizing factor found from the energy conservation requirement. The denominator is not easily separated into stochastic and deterministic parts. However the integration over all possible directions in finding the total scattered energy will generally diminish the influence of surface statistics. A closer look into the energy redistribution follows from the bistatic scatter diagram.

From Appendix II it is known that the general bistatic form of $\sigma_{CSM(1)}$ follows from (3) by replacing $\cos 2\Delta I$ by $\cos(\Delta I + \Delta S)$ where the scatter phase term ΔS equals ΔI given in (2) except for θ being replaced by the scatter angle θ'. In the special cases $\theta' = \pi \pm \theta$ the height dependent terms of ΔI and ΔS cancel. For $\theta' = \pi - \theta$ the numerator of $\sigma_{CSM(1)}(\theta, \theta')$ equals $N^2\{(\sin u)/u\}^2$ with u given in (8). For $\theta' = \pi + \theta$ also the distance dependent

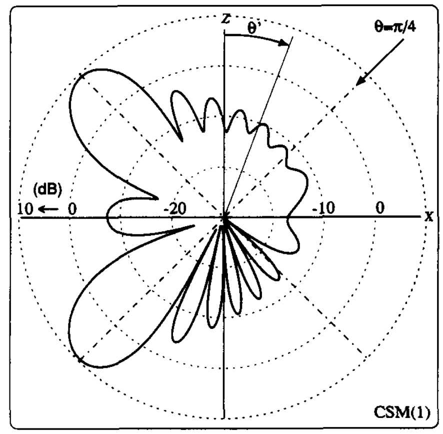

(a)

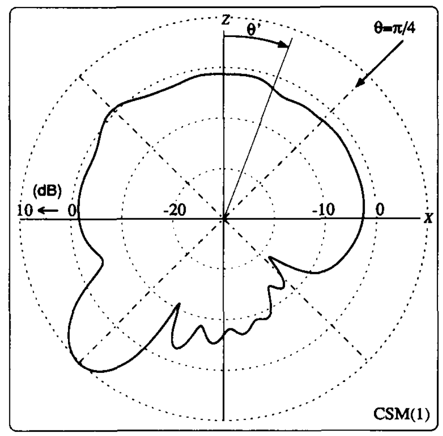

(b)

Fig. 7. (a) Bistatic scatter diagram $\sigma_{CSM(1)}(\theta, \theta')$ in dB for incidence angle $\theta = \pi/4$ with the scatter angle $0 < \theta' < 2\pi$, low roughness: $s = 0.03\lambda$, (b) idem, high roughness: $s = 0.3\lambda$.

terms cancel and the numerator equals its maximum value N^2 always.

These coherent scatter contributions are thus found to be present only in the half-space below the surface. Vice versa, the effect of surface roughness introducing incoherence will generally be strongest in the source half-space $-\pi/2 < \theta' < \pi/2$.

Examples of the bistatic scatter diagrams $\sigma_{CSM(1)}(\theta, \theta')$ are given in Figs. 7(a) and (b) for the low, respectively, high roughness cases $s = 0.03\lambda$ and $s = 0.3\lambda$, with model parameter values $\theta = \pi/4$, $L = 4\lambda$, $N = 16$ and averaging over 100 realizations. The increase of roughness leads to a decrease of symmetry with respect to the xy-plane, scattering on the incident side shows the strongest incoherence resulting in nearly isotropic behavior for $s = 0.3\lambda$ and, as explained before, associated with this the numerator of $\sigma_{CSM(1)}$ will be nearly equal to N.

For $\theta' = 3\pi/4$ the coherence effect does not lead to a strong scattering into this direction due to the mentioned factor $\{(\sin u)/u\}^2$. Also for $\theta' = 5\pi/4$ both cases show nearly the same scattering intensity which is now maximum always. The latter maximum value may be found by dividing N^2 by the value of the denominator. The resulting value is seen to be near 10 dB for both the $s = 0.03\lambda$ and the $s = 0.3\lambda$ case confirming that the effect of surface statistics on the denominator is relatively weak.

It is observed that the main lobe in the scatter diagram around $\theta' = \pi + \theta$, the forward scatter direction, reaches a certain limiting shape for N large enough and s constant. In this case most of the energy is concentrated in this coherent beam and its associated side lobes where the latter are for convenience omitted from this present discussion. If s is increased the main lobe narrows down so that it would contain less energy if N remains constant. This is only partly true because the scatter diagram area is kept constant by the denominator normalizing with respect to the total scattered energy. The major part of the energy will again appear in the main lobe so that its amplitude increases. The remaining energy will reinforce incoherent parts of the scatter diagram. Due to the latter N may subsequently be further increased to gather the "lost" energy back to the main lobe.

It is concluded that in case of random roughness without surface correlation an increase of the number of lines N will cause the result of the model to consist of coherent contributions only. These coherent contributions will progressively add to the forward scatter for increasing roughness. As a consequence the backscatter will vanish as seen, e.g., in Fig. 2 where it is noted that the one-dimensional, line version of the model essentially works the same as the point scatterer model.

IV. Verification

The models introduced above present a simplified approach in solving radar surface scattering problems. They are to be verified by measurements and compared with other theoretical solutions of the scatterers problem. Indoor Radar Cross Section (RCS) measurements confirm the correctness of accounting for electromagnetic coupling effects between two scatterers in function of the distance between them by applying the principle of energy conservation.

The RCS-measurement facility forms part of the Delft University of Technology Chamber for Antenna Tests (DUCAT) providing an electromagnetically anechoic and well-shielded environment of $6 \times 3 \times 3$ m^3. The equipment consists of a HP 8510B network analyzer controlling a synthesizer and sweeper source in combination with a test-set developed at Delft University and using a so-called external mixer configuration. A laser is used as a reference in target positioning. Further details can be found in [5], [6]. DUCAT includes the possibility of performing bistatic measurements where the transmit antenna remains fixed and the receiver antenna is moved in a circle around the target.

For model verification purposes numerically solving the electric field integral equation (EFIE) of the scattering problem with the Method of Moments (MOM) is used. The far zone scattered field and subsequently the power can then be computed. Specifically, the EFIE formulation of the scattering from a *wire object*, such as a straight needle and an array of parallel needles is numerically solved and the CSM model result is compared with the MOM solution.

A. Coupling Constant

The model equation given in (3) applied to the case with only two lines is rewritten in accordance with Appendix II into

$$\sigma_{CSM(1)} = \frac{\sigma_2^c}{2\sigma^c} = (1 + \cos\{\beta d(\sin\theta + \sin\theta')\}) \cdot C(\theta) \tag{11}$$

where σ_2^c denotes the scattering width or radar cross section per unit length of a combination of two parallel line scatterers of infinite length.

It is noted that (11) gives a bistatic form of $\sigma_{CSM(1)}$ for the case where the line scatterer heights with respect to the xy-plane are zero.

The model result given in (11) is compared to measurement in Fig. 8. The measurements are bistatic due to the use of two antennas. Setting the distance between the antennas at 0.2 m and their distance to the target plane to 1.5 m leads to the bistatic situation $\theta = -\theta' = 4°$. In this case the right-hand side of (11) reduces to $2 \cdot C(4°)$ which is given by the upper solid curve in Fig. 8. The bistatic angle effect is found to cause a relatively smooth part in the otherwise oscillatory coupling factor C in function of the line distance d.

The two lower curves in Fig. 8 present measurement results at 10 GHz using two metallic needles in a measurement setup conform the (infinite length) two line model geometry to which (11) applies. The needles are oriented parallel to the polarization direction. The distance d between the needles was varied from 0 to 10λ. The dotted curves concern half a wavelength long needles and the dashed ones concern one λ long needles, with diameters of $\frac{1}{4}$ and $\frac{1}{2}$ mm, respectively.

The two-needle measurements are corrected for the antenna diagram influence. As a result the two lower curves are in close agreement with the upper theoretical one. The main conclusion is that these measurements clearly support the description of the electromagnetic coupling between two line scatterers as given in Appendix II using the energy conservation principle. As such it is a basic step in validating the general model formulation.

The discussion of the experimental results is however not yet complete. The needles have finite length and theory is based on lines of infinite length. Using longer needles presents difficulties in maintaining that their illumination is essentially that of a plane wave as required. Still, deviations of the two-needle measurements from the theoretical prediction are relatively small, especially for

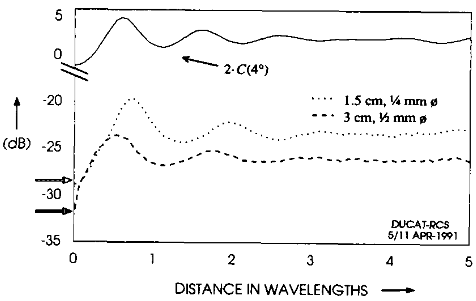

Fig. 8. The coupling in dB between two line scatterers, model and measurement: Predicted result for bistatic angle $\theta = -\theta' = 4°$ (solid curve). Measurement results using two needles of $\frac{1}{2}\lambda$ length (dotted curve), resp., λ length (dashed curve). The arrows next to the vertical scale point to the measured values of one $\frac{1}{2}\lambda$ needle (upper) and one λ needle (lower).

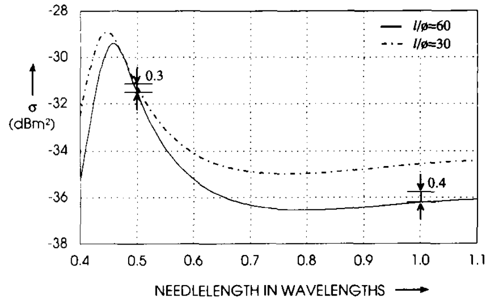

Fig. 9. Radar cross section in dBm^2 of a single needle scatterer as a function of needle length l for length diameter ratio $l/\varnothing = 60$ and 30 (according to Van Vleck *et. al.* [7, p. 290]); indicated are the differences with the measured single needle values.

the λ length case. Compared to the latter the $\frac{1}{2}\lambda$ result exhibits an offset with respect to both the horizontal and the vertical scale. Furthermore both two-needle results are found to converge to their respective one-needle backscatter values if the distance becomes close to zero. These values are 3 dB lower than theory predicts. But then in theory the two lines never reduce to one for $d \rightarrow 0$, whereas in practice the needles will touch and form a one ''needle''-combination.

The observations mentioned above may to a large extent be explained by calculating the needle backscatter in function of needle length l and needle diameter $\varnothing$ using a method described by Van Vleck *et al.* [7]. As a result the behavior of the radar cross section versus needle length is given in Fig. 9. The solid curve is obtained for the length diameter ratio $l/\varnothing$ equal to 60 that is the actual values of the needles used. The other curve gives the double diameter case, where $l/\varnothing = 30$, used to approximate the case of two touching needles. Both curves reveal the presence of a needle resonance peak around a value slightly lower than $l/\lambda = 0.5$. This explains the vertical offset of the $\frac{1}{2}\lambda$ two-needle curve in Fig. 8 and the resonance effect probably also causes the noted horizontal offset. The absolute differences between the measured values in the one-needle cases at zero position compared to the calculation results are found to be 0.3 and 0.4 dB for the $\frac{1}{2}\lambda$, respectively, λ needles.

Doubling of the diameter $\varnothing$ clearly affects the $\frac{1}{2}\lambda$ length result much less than the λ result, as can be seen in Fig. 9. This agrees with the behavior of both two-needle curves in Fig. 8 around zero distance. The two-needle $\frac{1}{2}\lambda$ curve was already noticed to be horizontally offset and in combination with this there is a quite gradual convergence to the value that was found for one such a needle, if the needle distance reduces to zero. The two-needle λ curve converges to a 2 dB higher value as found for one λ needle and only very close to zero distance it rather discontinuously assumes the one-needle λ result. From this it may be concluded that the mechanical alignment is possibly not that perfect to guarantee that, e.g., the needles are still exactly next to each other.

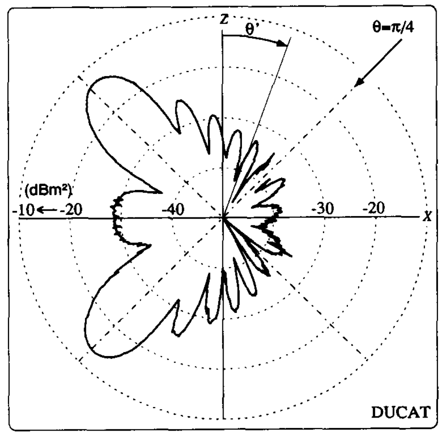

Fig. 10. Measured bistatic RCS in dBm^2, $N = 16$ needles, no roughness.

B. Measurement and Methods of Moments

A bistatic measurement result for a target consisting of an array of $N = 16$ parallel metallic needles is presented in Fig. 10. The needle lengths equal the wavelength, $\lambda = 3$ cm, their diameters are $\frac{1}{2}$ mm, and the needle spacing $d = 8$ mm. Only the flat case is considered, i.e., the needle heights are set to zero. The polarization of the transmitter and receiver are both parallel to the needle axes. The incidence angle is fixed at 45 degrees. Measurement sensitivity mainly depends on the cross-talk level between the antennas and is a function of their relative positions. Measurement reproducibility was found to be typically within 0.2 dB.

The scattering from the needles can be calculated by numerically solving the electric field integral formulation of the problem with the Method of Moments [8]. The bistatic RCS result for the flat case considered above is presented in Fig. 11 and is in perfect agreement with the previously given measurement result in Fig. 10.

Use of MOM avoids performing measurements that become laborious in the case of varying needle heights when roughness is introduced. On the other hand actually solv-

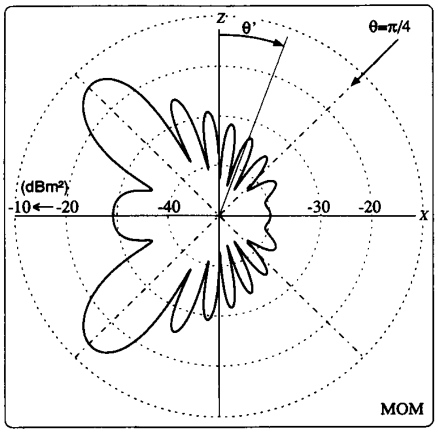

Fig. 11. Bistatic RCS in dBm² from Method of Moments, $N = 16$ needles, no roughness.

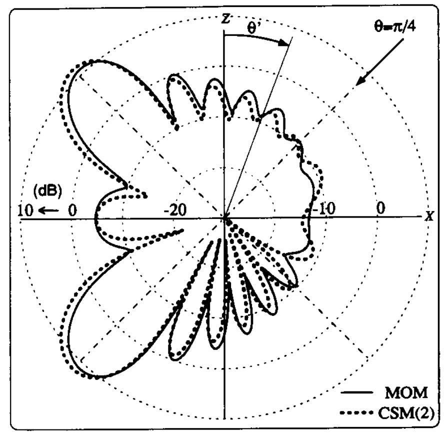

(a)

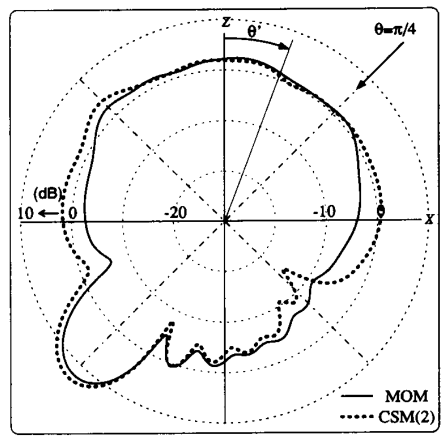

(b)

Fig. 12. (a) Bistatic scatter diagrams σ_{MOM} and $\sigma_{CSM(2)}$ in dB, $N = 16$, low roughness: $s = 0.03\lambda$, (b) idem, high roughness: $s = 0.3\lambda$.

ing the scatter problem has the disadvantage of relatively high computer memory and time requirement. In the next, model results are compared with those calculated with MOM.

To enable comparison the MOM result is normalized to give the bistatic scatter diagram, $\sigma_{MOM}(\theta, \theta')$, in the same way as the model [8, p. 76]. The two-dimensional model is used to be able to account for the finite length of the needles.

Following the example given in Section III-B, the bistatic scatterdiagrams $\sigma_{MOM}(\theta, \theta')$ and $\sigma_{CSM(2)}(\theta, \theta')$ are given in Fig. 12(a) for the low roughness case $s = 0.03\lambda$ and likewise for the high roughness case $s = 0.3\lambda$ in Fig. 12(b). As before, averaging is performed over 100 realizations, the incidence angle $\theta = \pi/4$, and $N = 16$ needles of length λ are used with a $\lambda/4$ grid spacing.

Figs. 12(a), (b) show that the model (dotted line) behaves quite well for the chosen settings. For both roughness cases the modeled backscatter nearly equals the MOM result (solid line). The main differences are found in the "end-fire" directions, $\theta' = \pi/2$ and $\theta' = 3\pi/2$, where the model results become too high when roughness is increased. This disagreement is caused by the fact that the model only accounts for phase differences between the scattered field contributions in a given realization depending on propagation path length differences. The modeled scattered field is similar to that of the method of moments expression obtained from the far-zone magnetic vector potential after substituting the needle currents. They differ however in that MOM accounts for additional phase and also amplitude differences between the scattered field contributions that is due to the current distributions.

V. Conclusion

A coupled scatterer model is derived to simulate radar scattering from distributed targets. To enable fast evaluation of model parameter influences a one-dimensional version of the model is given. The model formulation is straightforward and simple limiting cases show expected results. The coupling between the scatterers in the model is based on the energy conservation requirement assuming perfect conductivity. This coupling was experimentally verified using a two-needle configuration. In further verification the number of scatterers is increased and scatterer height is made variable. Bistatic scatter diagram results obtained with the model are found to agree well with Method of Moments results.

Appendix I
Two-Dimensional Model Formulation

The two-dimensional model geometry is presented in Fig. 13. A plane wave is incident on a rectangular surface built up of K identical lossless point scatterers that are spaced d_a in x-direction and d_b in y-direction. The incident propagation direction is given by the angles θ and ϕ. In the next only the case $\phi = 0$ will be considered. The point scatterers are assumed to scatter isotropically, their heights with respect to the plane $z = 0$ may vary.

The phase relations between the scatter contributions of the different points depend on their relative positions. For

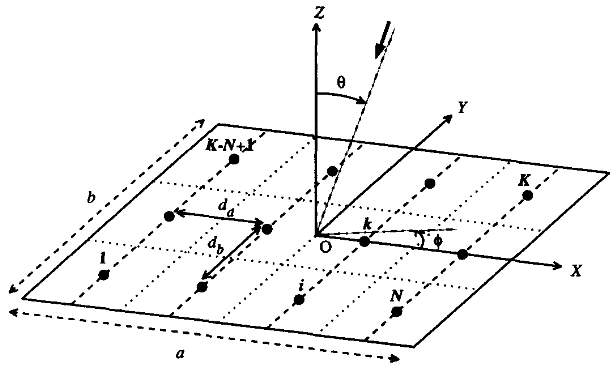

Fig. 13. Two-dimensional, point scatterer, model geometry.

the total phase difference between the scatter contribution of point k and that of reference point 1 we can write

$$\varphi_k = I_k + S_k \tag{A1}$$

$$I_k = \beta(d_{ai} \sin\theta + h_k \cos\theta) \tag{A2}$$

$$S_k = \beta((d_{ai} \cos\phi' + d_{bj} \sin\phi') \sin\theta' + h_k \cos\theta') \tag{A3}$$

where $\beta = 2\pi/\lambda$ with λ the radar wavelength, the angles θ' and ϕ' give the scattered wave propagation direction and (d_{ai}, d_{bj}, h_k) is the position vector from point 1 to point k. Let the amount of power intercepted by each point scatterer be equal. It follows that the scattered electrical field on a large distance r can be written as

$$E^s = \sum_{k=1}^{K} E_k^s \quad \text{with} \quad E_k^s = Q \frac{\exp(-j\beta r)}{r} \exp(j\varphi_k) \tag{A4}$$

where Q is a constant that is related to the total scattered power. From (A4) it follows that

$$\begin{aligned} \frac{r^2}{Q^2} |E^s|^2 &= \left(\sum_{k=1}^{K} \cos\varphi_k\right)^2 + \left(\sum_{k=1}^{K} \sin\varphi_k\right)^2 \\ &= K + 2\sum_{k=1}^{K} \sum_{k'=k+1}^{K} \cos\varphi_{kk'} \\ &= K + 2\sum_{k=1}^{K} \sum_{k'=k+1}^{K} \cos I_{kk'} \cos S_{kk'} \\ &\quad - 2\sum_{k=1}^{K} \sum_{k'=k+1}^{K} \sin I_{kk'} \sin S_{kk'} \end{aligned} \tag{A5}$$

with

$$\varphi_{kk'} = \varphi_k - \varphi_{k'} = I_{kk'} + S_{kk'} \tag{A6}$$

$$I_{kk'} = \beta((d_{ai} - d_{ai'}) \sin\theta + (h_k - h_{k'}) \cos\theta) \tag{A7}$$

$$\begin{aligned} S_{kk'} = \beta(&\{(d_{ai} - d_{ai'}) \cos\phi' + (d_{bj} - d_{bj'}) \sin\phi'\} \\ &\cdot \sin\theta' + (h_k - h_{k'}) \cos\theta'). \end{aligned} \tag{A8}$$

From (A5) it is concluded that in addition to the term K which is due to the points themselves, a summation of interaction terms between all possible point pairs is found. The total scattered power is calculated by integrating over a sphere with radius r:

$$\begin{aligned} P &= \int_0^{\pi} \int_0^{2\pi} \frac{\frac{1}{2}|E^s|^2}{120\pi} r^2 \sin\theta' \, d\theta' \, d\phi' \\ &= \frac{Q^2}{60} \left(K + 2\sum_{k=1}^{K} \sum_{k'=k+1}^{K} \cos I_{kk'} S_P^e \right. \\ &\quad \left. - 2\sum_{k=1}^{K} \sum_{k'=k+1}^{K} \sin I_{kk'} S_P^o \right) \end{aligned} \tag{A9}$$

where S_P^e and S_P^o denote even, respectively, odd point scatter integration terms, that after integration with respect to ϕ' become

$$\begin{aligned} S_P^e &= \tfrac{1}{2} \int_0^{\pi} \cos(H \cos\theta') J_0(D \sin\theta') \sin\theta' \, d\theta' \\ &= S_P^{e,\text{upper}} + S_P^{e,\text{lower}} \end{aligned} \tag{A10}$$

$$\begin{aligned} S_P^o &= \tfrac{1}{2} \int_0^{\pi} \sin(H \cos\theta') J_0(D \sin\theta') \sin\theta' \, d\theta' \\ &= S_P^{o,\text{upper}} + S_P^{o,\text{lower}} = 0 \end{aligned} \tag{A11}$$

where J_0 is the Bessel function of the first kind and zero order, H and D are phase differences between point scatterers k and k':

$$H = \beta(h_k - h_{k'}), \quad D = \beta\sqrt{(d_{ai} - d_{ai'})^2 + (d_{bj} - d_{bj'})^2} \tag{A12}$$

furthermore (A10) and (A11) are written as the sum of two integrals over the half-space above, respectively, below the xy-plane, i.e., $\theta' = \pi/2$. These two integrals are equal in the even, symmetric case whereas they cancel in the odd, asymmetric case. The remaining expression (A10) can be solved according to Gradshteyn [9] resulting in

$$S_P^e = 2S_P^{e,\text{upper}} = 2S_P^{e,\text{lower}} = \frac{\sin\sqrt{D^2 + H^2}}{\sqrt{D^2 + H^2}}. \tag{A13}$$

With (A9), (A12), and (A13) the total scattered power becomes

$$P = \frac{Q^2}{60} \left(K + 2\sum_{k=1}^{K} \sum_{k'=k+1}^{K} \cos I_{kk'} \frac{\sin R_{kk'}}{R_{kk'}}\right) \tag{A14}$$

with $R_{kk'}$ given by

$$R_{kk'} = \beta\sqrt{(d_{ai} - d_{ai'})^2 + (d_{bj} - d_{bj'})^2 + (h_k - h_{k'})^2}. \tag{A15}$$

The input power is assumed to be fully intercepted by the point scatterers. Since there is no loss of energy, the total scattered power must be equal to the input power. The input power is given by

$$P = K\sigma \frac{\frac{1}{2}|E^i|^2}{120\pi} \tag{A16}$$

where σ is the radar cross section of an isolated point scatterer and E^i the incident electric field. The radar cross section follows as

$$\sigma_P = \lim_{r\to\infty} 4\pi r^2 \frac{|E^s|^2}{|E^i|^2} = \lim_{r\to\infty} K\sigma \frac{r^2}{60P} |E^s|^2 \tag{A17}$$

and $|E^s|$ is obtained by combining (A5) with (A14) through elimination of the constant Q. The radar cross section normalized with respect to the total point scatterer cross section, $K\sigma$, derived from the two-dimensional coupled scatterer model is given by

$$\sigma_{CSM(2)}(\theta, \theta') = \frac{\sigma_P}{K\sigma} = \frac{K + 2 \sum_{k=1}^{K} \sum_{k'=k+1}^{K} \cos(I_{kk'} + S_{kk'})}{K + 2 \sum_{k=1}^{K} \sum_{k'=k+1}^{K} \cos I_{kk'} \frac{\sin R_{kk'}}{R_{kk'}}}. \tag{A18}$$

Appendix II
Coupling Between Two Line Scatterers, The One-Dimensional Model

The one-dimensional model formulation may be given in close analogy in Appendix I. An alternative approach however is preferred to accentuate the coupling between two—in this case—line scatterers that arises if their mutual distance becomes small with respect to the radar wavelength. The two line case is thereafter easily related to the line scatterer model version with N equally spaced identical line scatterers placed parallel to each other including possible height differences representing one-dimensionally rough structures.

A. Two Line Scatterers

Assuming an incident plane wave with electric field E^i parallel to an isolated line scatterer the latter will intercept power $\sigma^c S$ per unit length where

$$S = \frac{\frac{1}{2}|E^i|^2}{120\pi} \tag{A19}$$

is the power density of the incoming wave and

$$\sigma^c = \lim_{r\to\infty} 2\pi r \frac{|E^s|^2}{|E^i|^2} \tag{A20}$$

the scattering width or radar cross section per unit length, E^s is the scattered electric field.

An identical second line scatterer placed parallel to the first one at distance d will intercept $\sigma^c S$ per unit length as well. As long as there is no electromagnetic coupling each

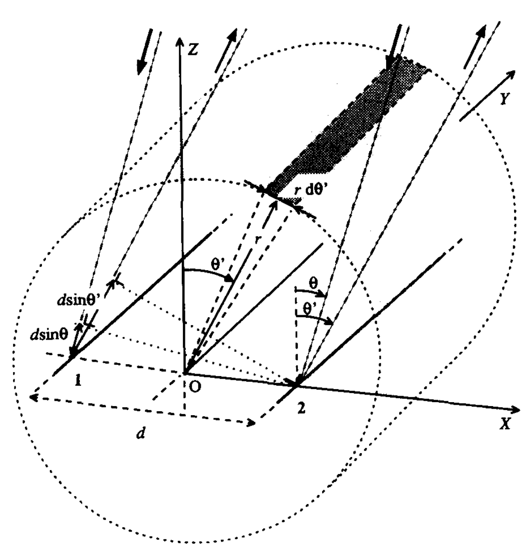

Fig. 14. Two line scatterer bistatic radar geometry.

line scatterer will scatter isotropically around its axis. It can be shown then that, for the general bistatic case given in Fig. 14, the scattered electric field component E_1 at large distance r of scatterer 1 in the direction θ' can be written as

$$E_1 = \sqrt{120\sigma^c S} \frac{\exp(-j\beta r)}{\sqrt{r}} \tag{A21}$$

and that of scatterer 2 by

$$E_2 = \sqrt{120\sigma^c S} \frac{\exp(-j\beta r)}{\sqrt{r}} \exp\{j\beta d(\sin\theta + \sin\theta')\} \tag{A22}$$

where $\beta = 2\pi/\lambda$ and θ represents the incidence angle of the illuminating wave. To find the total scattered power P per unit length $|E^s|^2 = |E_1 + E_2|^2$ is integrated over a cylinder. Since the line scatterers are parallel to the y-axis, unit length surface elements of width $r\,d\theta'$ can be used so that

$$P = \int_0^{2\pi} \frac{\frac{1}{2}|E^s|^2}{120\pi} r\,d\theta' = 2\sigma^c S\{1 + \cos(\beta d \sin\theta) J_0(\beta d)\} \tag{A23}$$

with J_0 the Bessel function of the first kind and zero order. This result shows that the total scattered power P may become larger as well as smaller than the input power $2\sigma^c S$, thus energy conservation has to be set as a requirement. This may be implemented by assuming that, due to coupling, the radar cross section of the line scatterers is modified by a factor C. As a result the right-hand side of (A23) has to be multiplied by the same factor. When subsequently in the lossless case P is set equal to the input power $2\sigma^c S$ it is found that

$$C = \{1 + \cos(\beta d \sin\theta) J_0(\beta d)\}^{-1}. \tag{A24}$$

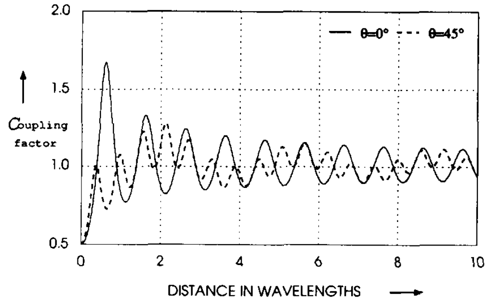

Fig. 15. Coupling factor between two line scatterers for incidence angle $\theta = 0°$ and $\theta = 45°$.

The factor C that describes the electromagnetic coupling effect is shown in Fig. 15 as a function of the separation distance d for two values of the incidence angle θ. The factor C approaches unity for large d/λ and is equal to 1 for $d/\lambda = m/2 - 1/8$ ($m = 1, 2, \cdots$) whereas $d/\lambda = 0$ results in $C = \frac{1}{2}$.

From a physical point of view (A24) may be interpreted as that the line scatterers are no longer scattering isotropically around their axes. Consequently also the spatial distribution of the power scattered by the combination of the two line scatterers will be influenced. Once the modified radar cross section $C\sigma^c$ of the line scatterers is known, one obtains, using (A21) and (A22)

$$|E^s|^2 = \frac{240\sigma^c S}{r} \frac{1 + \cos\{\beta d(\sin\theta + \sin\theta')\}}{1 + \cos(\beta d \sin\theta) J_0(\beta d)}. \quad \text{(A25)}$$

Finally using (A19) and (A20) the radar cross section per unit length of the combination of the two line scatterers is found:

$$\sigma_2^c = 2\sigma^c \frac{1 + \cos\{\beta d(\sin\theta + \sin\theta')\}}{1 + \cos(\beta d \sin\theta) J_0(\beta d)}. \quad \text{(A26)}$$

For $d/\lambda = 0$ the line scatterers are coinciding and in this case $\sigma_2^c = 2\sigma^c$. In the other limiting case $d/\lambda \to \infty$, σ_2^c is varying between 0 and $4\sigma^c$ as a function of θ and θ'.

B. One-Dimensional Model

The two line case may be generalized to the one-dimensional model, based on N parallel line scatterers (Fig. 4), by combining the scattered power expression given in (A23) and the one given in Appendix I (A9) for the point scatterer case into

$$P = N\sigma^c S \left(1 + \frac{2}{N} \sum_{k=1}^{N} \sum_{k'=k+1}^{N} \cos I_{kk'} S_L^e - \frac{2}{N} \sum_{k=1}^{N} \sum_{k'=k+1}^{N} \sin I_{kk'} S_L^o \right) \quad \text{(A27)}$$

where the even and odd scatter integration terms for the line target case are given, respectively, by

$$S_L^e = \frac{1}{2\pi} \int_0^{2\pi} \cos S_{kk'}\, d\theta'$$

$$= \frac{1}{\pi} \int_0^{\pi} \cos(H \cos\theta') \cos(D \sin\theta')\, d\theta' \quad \text{(A28)}$$

$$S_L^o = \frac{1}{2\pi} \int_0^{2\pi} \sin S_{kk'}\, d\theta'$$

$$= \frac{1}{\pi} \int_0^{\pi} \sin(H \cos\theta') \cos(D \cos\theta')\, d\theta' \quad \text{(A29)}$$

and

$$I_{kk'} = \beta((d_k - d_{k'}) \sin\theta + (h_k - h_{k'}) \cos\theta) \quad \text{(A30)}$$

$$S_{kk'} = \beta((d_k - d_{k'}) \sin\theta' + (h_k - h_{k'}) \cos\theta') \quad \text{(A31)}$$

$$H = \beta(h_k - h_{k'}), \qquad D = \beta(d_k - d_{k'}). \quad \text{(A32)}$$

The odd scatter integration term (A29) has an asymmetry in the integrand with respect to $\theta' = \pi/2$ so that the upper and lower half-space contributions cancel out. The remaining expression (A28) is solved by substituting $H = D\tan(\alpha)$ into

$$S_L^e = 2S_L^{e,\text{upper}} = 2S_L^{e,\text{lower}} = J_0(\sqrt{D^2 + H^2}). \quad \text{(A33)}$$

The scattered power expression therefore becomes

$$P = N\sigma^c S \left(1 + \frac{2}{N} \sum_{k=1}^{N} \sum_{k'=k+1}^{N} \cos I_{kk'} J_0(R_{kk'}) \right)$$

$$= N\sigma^c S \cdot C_N^{-1} \quad \text{(A34)}$$

of which (A23) follows as a special case for $N = 2$ and zero height difference. Furthermore P equals the input power $N\sigma^c S$ after multiplying σ^c with the coupling factor C_N. The far-field scattered electrical field was initially, i.e., in the absence of coupling, characterized by

$$|E^s|^2 = \frac{120 N\sigma^c S}{r} \left(1 + \frac{2}{N} \sum_{k=1}^{N} \sum_{k'=k+1}^{N} \cos(I_{kk'} + S_{kk'}) \right). \quad \text{(A35)}$$

The coupling effects are accounted for by replacing σ^c by $C_N \sigma^c$ in the expression above. Then, using (A19) and (A20), the radar cross section per unit length of the combination of N line scatterers is

$$\sigma_L^c = \lim_{r \to \infty} 2\pi r \frac{|E^s|^2}{|E^i|^2} = \lim_{r \to \infty} N\sigma^c \frac{r}{120P} |E^s|^2 \quad \text{(A36)}$$

and in accordance with Appendix I (A18) the radar cross section normalized with respect to the total line scatterer cross section, $N\sigma^c$, derived from the one-dimensional coupled scatterer model is given by

$$\sigma_{CSM(1)}(\theta, \theta') = \frac{\sigma_L^c}{N\sigma^c} = \frac{N + 2\sum_{k=1}^{N} \sum_{k'=k+1}^{N} \cos(I_{kk'} + S_{kk'})}{N + 2\sum_{k=1}^{N} \sum_{k'=k+1}^{N} \cos I_{kk'} J_0(R_{kk'})}. \quad \text{(A37)}$$

Acknowledgment

The authors would like to express their special thanks to M. van Sliedregt and L. Krul for their contributions and constructive comments on the research presented in this paper.

References

[1] F. T. Ulaby, R. K. Moore, and A. K. Fung, *Microwave Remote Sensing*. London: Addison-Wesley, vol. 2, 1982, ch. 7.

[2] E. P. W. Attema, P. J. van Kats, and L. Krul, "A radar signature model for partially coherent scattering from irregular surfaces," *IEEE Trans. Geosci. Remote Sensing*, vol. 20, no. 1, pp. 76–84, 1982.

[3] P. Beckmann and A. Spizzichino, *The Scattering of Electromagnetic Waves from Rough Surfaces*. Norwood, MA: Artech House, 1987, p. 147.

[4] G. T. Ruck, D. E. Barrick, W. D. Stuart, and C. K. Krichbaum, *Radar Cross Section Handbook*, vol. 2. New York: Plenum, 1970, p. 523.

[5] P. J. F. Swart, E. Janse, and P. Snoeij, "RCS backscatter measurements of very small objects for backscatter model verification," in *Proc. CICR-91*, Beijing, China, Oct. 22–24, 1991, pp. 576–579.

[6] P. J. F. Swart and P. Snoeij, "Point target simulation verification using low level RCS measurements," in *Proc. IGARSS'91*, Helsinki, Finland, 1991, pp. 599–602.

[7] J. H. Van Vleck, F. Bloch, and M. Hamermesh, "Theory of radar reflection from wires or thin metallic strips," *J. Appl. Phys.*, vol. 18, pp. 274–294, p. 290, 1947.

[8] R. F. Harrington, *Field Computation by Moment Methods*. New York: Macmillan, 1968, ch. 4.

[9] I. S. Gradshteyn and I. M. Ryzhik, *Tables of Integrals, Series, and Products* (corr. and enl. ed.). New York: Academic, 1980, p. 737.

Peter J. F. Swart was born in Amsterdam, The Netherlands, on September 17, 1960. He received the M.Sc. degree in electrical engineering from The Delft University of Technology, The Netherlands, in 1985.

Since then he has been active in several areas of microwave remote sensing, including data processing, modeling, and in-door RCS measurements.

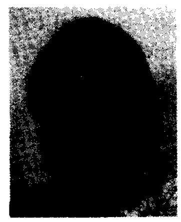

Paul Snoeij was born in Rotterdam, The Netherlands, on May 5, 1953. He received the M.Sc. degree in electrical engineering in 1982 from The Delft University of Technology, Delft, The Netherlands.

He joined the Delft University of Technology in 1978. Since 1981 he has been working on microwave remote sensing, with special emphasis on the design of SLAR, SAR, and scatterometer systems and on object-sensor interaction studies for the design of optimum sensors.